ORIGINAL PAPER

A Meso/Macroscale Theoretical Model for Investigating the Large Deformation of Soft Rock Tunnels Considering Creep and Anisotropic Effects

Chang Xia[1,2,3] · **Zhen Liu**[1,2,3] · **Cuiying Zhou**[1,2,3] · **Lihai Zhang**[4]

Abstract

The rheological deformation of soft rock resulting from tunnel excavation can lead to significant construction and safety challenges. In this study, a multiphase numerical model was developed to simulate the rheological deformation of soft rock surrounding a tunnel after excavation. The developed model considers the coupled meso/macroscale creep and damage processes of the rock using the coupled discrete element method–finite element method (DEM–FEM). In particular, the damage and deformation accumulation at the mesoscale (i.e., initial phase before excavation, loading phase due to the disturbance of the excavation and creep-induced damage phase leading to large deformation) were incorporated into the model. The model predictions were validated using field monitoring data. By incorporating the coupled meso/macroscale deformation process of the rock into the model, the predicted time-dependent displacements of the tunnel face agree reasonably well with the monitoring data. In addition, the results demonstrate that tunnel brittle damage accumulated in mineral clusters severely leads to instantaneous deformation, which becomes less important in the creep evolution stage. Furthermore, the results indicate that the final deformation is characterized by a high sensitivity to the value of mesoscale modeling parameters.

Highlights

- A multiphase numerical model was developed to simulate the rheological deformation of soft rock surrounding a tunnel after excavation. The developed model considers the coupled meso/macroscale creep and damage process of the rock using the discrete element–finite element coupling method (DEM–FEM).
- By incorporating the coupled meso/macroscale deformation process of the rock into the model, the predicted time-dependent displacements of the tunnel face agree reasonably well with the monitoring data.
- Bedding joints were considered in the model, and the influences of joints on the local movement of grains as well as the final converged deformation were assessed.
- The influences of mesoscale tensile strength, mesoscale cohesive strength and the fraction of grains experiencing creep on macroscale deformation were discussed.

✉ Zhen Liu
liuzh8@mail.sysu.edu.cn

✉ Cuiying Zhou
zhoucy@mail.sysu.edu.cn

1   School of Civil Engineering, Sun Yat-Sen University,
    Zhuhai 519082, China

2   Guangdong Engineering Research Centre for Major
    Infrastructure Safety, Guangzhou 510275, China

3   Research Center for Geotechnical Engineering
    and Information Technology, Sun Yat-Sen University,
    Guangzhou 510275, China

4   The University of Melbourne, Melbourne, VIC 3010,
    Australia

1 Introduction

The rheological deformation of surrounding rock caused by excavating soft rock tunnels can lead to significant construction and safety challenges due to creep-induced damage (Xu et al. 2012; Kabwe et al. 2020a, b). Therefore, it is necessary to study the time-dependent deformation mechanisms of the soft rock surrounding rock caused by tunnel excavation (Manchao 2014; Wang and Cai 2022a, b).

The ultimate large deformation of soft rock is a creep–damage coupled problem (Li and Tang 2015; Wang and Cai 2020; Xia et al. 2021a, b). Inspired by the fundamental understanding of rock creep and damage mechanics, previous studies have mainly focused on the macroscale level using creep–damage constitutive models to reveal the rheological process of soft rock tunnels (Ping et al. 2016; Liu et al. 2017; Huang et al. 2020a, b; Li et al. 2022a, b, 2023). In addition, the different stages of long-term deformation of soft rocks were also studied from clay mineral slippage and disintegration (Fahimifar et al. 2010; Jiang et al. 2016; Liu et al. 2020a, b; Kovacevic et al. 2021; Maheshwari 2021; Cui et al. 2022). These results further demonstrate that the large deformation of soft rock tunnels is caused by the combined effects of damage and creep (Song et al. 2016; Yang et al. 2019; Kabwe et al. 2020a, b; Mu et al. 2020; Yu et al. 2020).

However, challenges remain in correlating the dissolution and slide of clay minerals at the mesoscale with crack propagation and coalescence at the macroscale. Long-term failure propagation in soft rock engineering is actually a multiscale issue (Li and Tang 2015; Xue et al. 2021). The mechanical properties and spatial orientations of rock joints could significantly influence tunnel excavation (Jia and Tang 2008; Deng et al. 2014). From a macroscopic perspective, joints may affect the local mineral grain flow and cause anisotropic deformation of the rock mass (Wang and Cai 2021a, b, 2022a). A multiscale analysis needs to be incorporated into the large deformation analysis of soft rock. Using a mesoscopic representative volume element (RVE), Tang et al. developed a theoretical model for simulating the trans-scale progressive failure of rock based on statistical and continuum damage mechanics (Li and Tang 2015). In addition, renormalization group theory (Xia et al. 2021a, b) and fractal geometry (Wei et al. 2019; Zhou et al. 2019) are commonly used to analyze meso-to-macro cascading in the phase-changing process, but they have limited capabilities of accurately predicting the deformation of the rocks surrounding the tunnel. Several attempts have been made to model the creep and time-dependent damage of soft rock from trans-scale modeling (Potyondy 2007; Li et al. 2017, 2018; Cui et al. 2019; Song et al. 2019; Guo et al. 2020; Wang and Cai 2021a, b; Xia et al. 2021a, b). However, the challenges of the computational efficiency and anisotropic nature of soft rock and rock joints need to be addressed before theoretical models can be implemented in engineering practice.

In the present study, a multiphase numerical model of soft rock was developed to investigate the creep-induced damage behavior of the soft rocks surrounding a tunnel after excavation through coupled meso/macroscale simulation. The anisotropic mechanical behavior of the rock due to joints was also considered. The numerical results of the developed model were validated by using the field monitoring data of a tunnel case study.

2 Methods

The discrete element method (DEM) can reproduce and characterize rock mechanical behavior. As one of the most widely used DEM software programs, Particle Flow Code (PFC) shows excellent performance in simulating the fabric features of rocks using multiple-grain models (Potyondy and Cundall 2004; Bahaaddini et al. 2013).

Rock deterioration is considered a micro-to-macro trans-scale process, where the accumulated internal mesoscale damage could lead to a macroscale strength loss. In this paper, we want to correlate mesoscopic damage to macroscopic large deformation. For rocks, microcracks initiate at the grain scale. The parallel bond model (PBM) implemented in PFC can simulate the cementation of spherical grains at contacts. Burger's model adopted in PFC can mimic the sliding creep of grains. The bond damage and grain creep are termed mesoscale damage herein. The mesoscale damage initiated from the grain contact area is limited at the mesoscale (less than 1 mm). The grain assembly can represent rock and rock mass, which are referred to as the macroscale (1–10 cm) and the engineering scale (> 1 m), respectively.
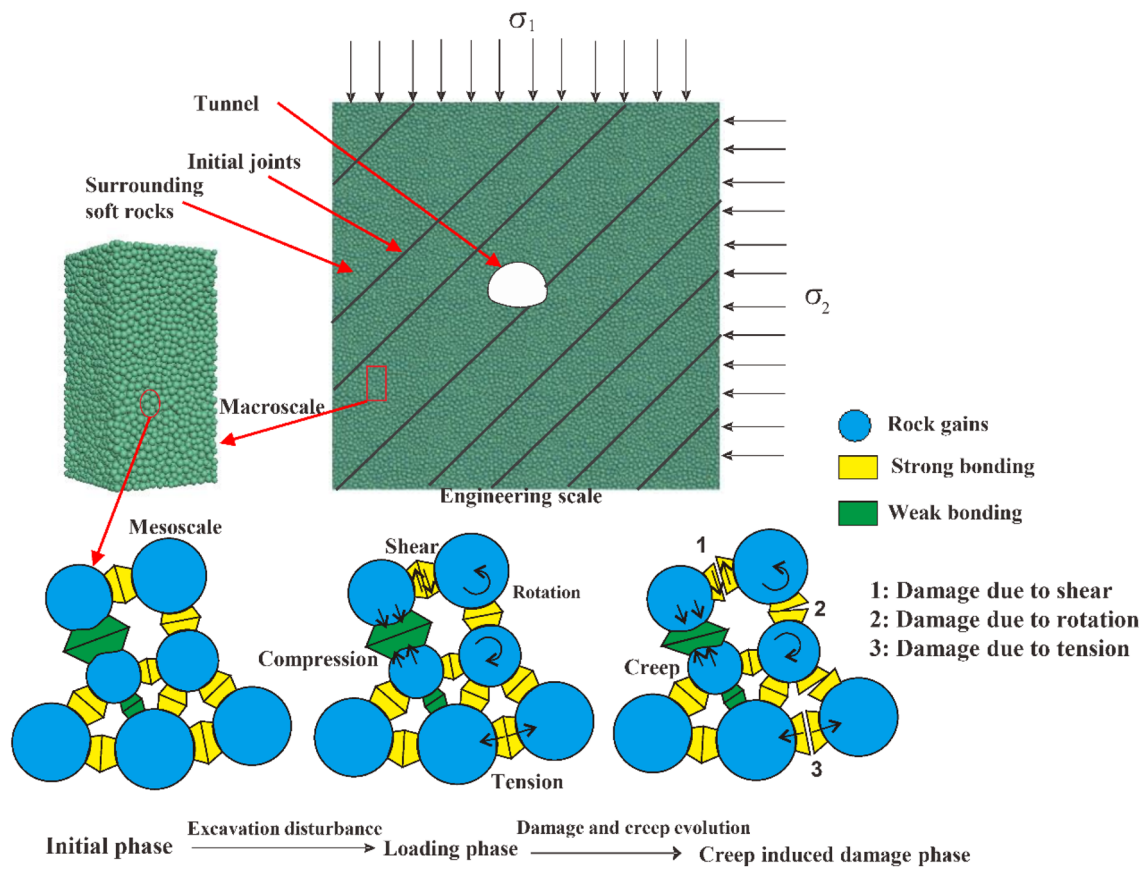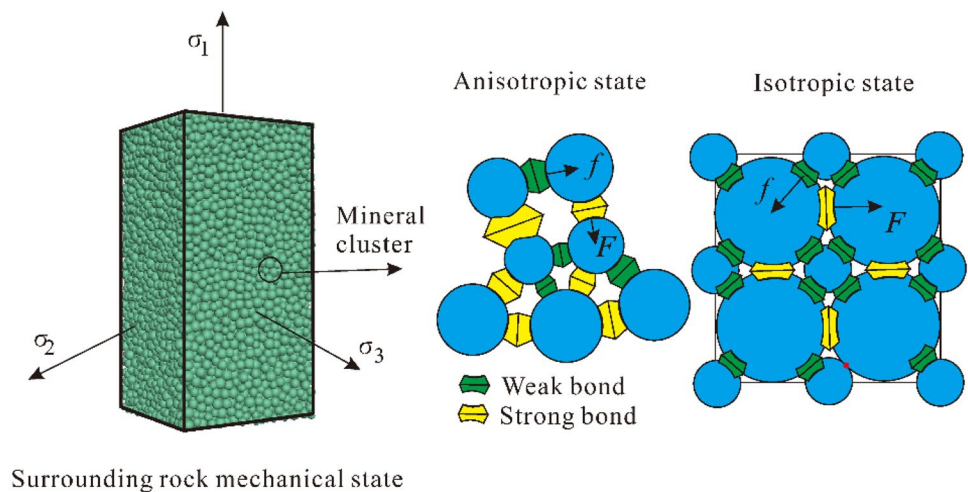
Fig. 1 Coupled meso/macroscale modeling of damage and deformation of the soft rock surrounding rock resulting from tunnel excavation

As shown in Fig. 1, the damage and deformation of the soft rock surrounding rock resulting from tunnel excavation can be studied through coupled meso/macroscale modeling. The mechanical properties of soft rock at the macroscale are characterized by bedrock strength, joint distribution, and tectonic stress, which are anisotropic in nature. The mechanical behavior of the rock at the mesoscale can be modeled by the skeleton and mineral bonding contents (Pinyol et al. 2007). In addition, the damage of the soft rock at the mesoscale can be divided into three phases: (1) initial phase before the excavation, (2) loading

Fig. 2 Macroscale modeling of soft rock with consideration of the anisotropic state

phase due to the excavation-induced stress redistribution, and (3) creep-induced damage and large deformation phase.

2.1 Modeling the Macroscale Damage and Deformation of the Surrounding Soft Rock Resulting from Tunnel Excavation

Figure 2 shows the macroscale modeling of the surrounding soft rock with consideration of the anisotropic state of the rock. The stress state of the soft rock surrounding the tunnel can be defined as:

$$\sigma_{ij} = \begin{bmatrix} \sigma_{11} & \sigma_{12} & \sigma_{13} \\ \sigma_{21} & \sigma_{22} & \sigma_{23} \\ \sigma_{31} & \sigma_{32} & \sigma_{33} \end{bmatrix}. \tag{1}$$

For hydrostatic conditions, the principal stresses of the surrounding rock can be described as:

$$\sigma_{ii} = \begin{bmatrix} \sigma_m & & \\ & \sigma_m & \\ & & \sigma_m \end{bmatrix}, \tag{2}$$

where $\sigma_m = \frac{1}{3}I_1 = \frac{1}{3}(\sigma_1 + \sigma_2 + \sigma_3)$ is the average principal stress. The stress tensor comprises the tectonic and gravity stresses of the rock surrounding the tunnel, which is composed of hydrostatic and deviatoric stresses. That is,

$$\sigma_{ij} = \delta_{ij}\sigma_m + s_{kk}, \tag{3}$$

where s_{kk} is the deviatoric stress tensor and δ_{ij} is the Kronecker delta (if $i = j$, $\delta_{ij} = 1$; if $i \neq j$, $\delta_{ij} = 0$). The damage process of the soft rock surrounding the tunnel can be treated as an irreversible dissipation process. The thermodynamic potential function ψ (Helmholtz energy) of the surrounding rock can be expressed as a function of elastic strain (ε^e) and internal variables, $v_k(k = 1, 2, 3 \dots, n)$, under isothermal conditions. That is,

$$\psi = \psi(\varepsilon^e, v_k), \tag{4a}$$

$$\sigma = \rho \frac{\partial \psi}{\partial \varepsilon^e}. \tag{4b}$$

The anisotropic damage characteristics of the rock can be defined using the isotropic hardening variable v_p for plastic deformation, the damage variable D for anisotropic damage, and the scalar variable β for the current state of damage. That is,

$$v_k = \{v_p, D, \beta\}. \tag{5}$$

In an engineering case, the rock mass has initial damage from rock mass joints (Fig. 1). Based on the strain equivalence principle, the strain caused by stress acting on damaged material in the stressed state is equivalent to the strain caused by effective stress acting on undamaged material, and we obtain:

$$\varepsilon = \frac{\sigma'}{E_0} = \frac{\sigma}{E_1}, \tag{6}$$

where E_0 and E_1 are the elastic moduli of intact and damaged rock, respectively. The damage variable D can be introduced as the decay of E_0 (Xue et al. 2022),

$$D = 1 - \frac{E_1}{E_0}. \tag{7}$$

Based on the irreversible thermodynamic theory (Zhou and Zhu 2010), it is assumed that the plastic deformation and damage evolution of soft rock are mutually independent. Thus, the Helmholtz free energy function of the surrounding soft rock can be described as:

$$\rho\psi(\varepsilon^e, v_p, D, \beta) = \rho\psi^e(\varepsilon_{ij}^e, D) + \rho\psi^p(v_p) + \rho\psi^d(\beta). \tag{8}$$

The term $\rho\psi^d(\beta)$ can be expressed in a simple form using the internal variable β, which represents damage accumulation and mesoscale damage evolution. Therefore, the damage potential function at the macroscale can be expressed as:

$$F_d(v_p, D, \beta) = 0, \tag{9}$$

$$d\beta = d\lambda_d \frac{\partial F_d}{\partial \beta}, \tag{10}$$

where λ_d is the parameter denoting the damage consistency parameter. If $F_d < 0$, the soft rock is in the elastic stage, and the stress tensor can be defined as Eq. (4b). In the damage stage, according to the non-associated rule of orthogonal flow, we obtain:

$$d\varepsilon_{ij}^d = d\lambda \frac{\partial Q}{\partial \sigma_{ij}}, \tag{11}$$

where Q denotes the damage yield function. λ is determined by the damage potential function F_d and the hardening parameter.

2.2 Modeling the Mesoscale Damage and Deformation of the Surrounding Soft Rock Resulting from Tunnel Excavation

To analyze the damage accumulation of soft rocks during tunnel excavation at the mesoscale, the following assumptions are made in this study:

(1) The tunnel rock is composed of skeleton particles and cementations (Pinyol et al. 2007; Li and Wong 2016).

(2) There are two types of bonding in soft rock, i.e., (1) strong bonding for tension, shear and torsion resistance and (2) weak bonding for creep resistance.

(3) Strong bonding fails when the bearing capacity is exceeded. Soft rocks experience creep when the slippage and dissipation of weak bonding occurs (Liu et al. 2020a, b).

2.2.1 Initial Phase Before the Excavation

Before excavation, the rock surrounding the tunnel is subject to tectonic in situ stress σ_{ij}, which is a stable and inelastic state. It is assumed that the total stress (σ_{ij}) can be expressed by the sum of the strong bonding stress (F_{ij}) and weak bonding stress (f_{ij}). That is,

$$\sigma_{ij} = F_{ij} + f_{ij} = 2f_{ij} + (F_{ij} - f_{ij}) = 2f_{ij} + \alpha_{kl} * F_{ij}, \tag{12}$$

where $\alpha_{kl} * F_{ij}$ is the anisotropic stress, which is expressed as $\beta_{kl} * f_{ij}$. α_{kl} and β_{kl} are tensors revealing anisotropy determined by the actual physical state of the rock surrounding the tunnel.

2.2.2 Loading Phase Due to Excavation-Induced Stress Redistribution

Due to tunnel excavation, the mechanical equilibrium of the surrounding rock is disturbed. As shown in Fig. 1, the cementations between grains play a role in resisting deformation caused by stress, preventing the relative shearing, deviation, and rotation of skeleton grains. The mesoscale damage can be described as the bonding failure of rock gains due to tension or shear, as shown in Fig. 3.
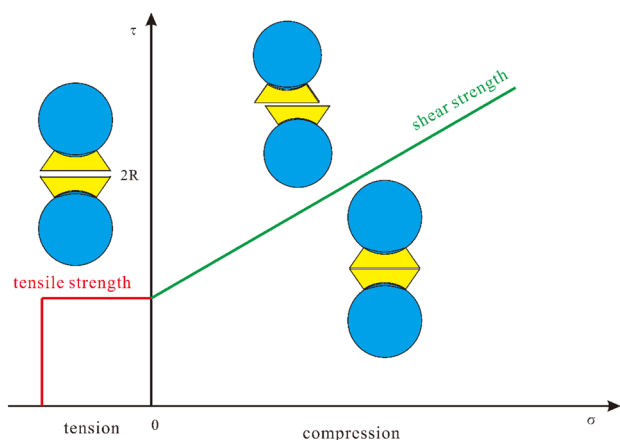

Fig. 3 Schematic diagram of the mesoscale damage model

The parallel bonded model (PBM) (Potyondy 2007; Xia et al. 2021a, b) is used for modeling the bonding failure of rock gains at the mesoscale mainly based on the binding characteristics of the rock gains, i.e., shear strength σ_c, tensile strength τ_c, normal stiffness k^n, tangential stiffness k^s, and bonding radius R. That is,

$$\Delta F^n = k^n A \Delta U^n, \Delta F^s = -k^s A \Delta U^s, \tag{13}$$

$$\Delta M^n = -k^s J \Delta \theta^n, \Delta M^s = -k^n I \Delta \theta^s, \tag{14}$$

where F^n and F^s are the normal and tangential forces, respectively. M^n and M^s are the normal and tangential moments, respectively. $U^n, U^s, \theta^n,$ and θ^s are the relative displacements and rotation angles in the normal and tangential directions, respectively. $A, I,$ and J are the area, moment of inertia, and polar moment of the bonds section, respectively, which can be described as

$$A = \pi R^2, \tag{15}$$

$$I = \frac{1}{4}\pi R^4, \tag{16}$$

$$J = \frac{1}{2}\pi R^4. \tag{17}$$

The maximum tensile stress and shear stress on the grain surface can be calculated using the following equations:

$$\sigma = \frac{-F^n}{A} + \frac{|M^s|R}{I}, \tag{18}$$

$$\tau = \frac{F^s}{A} + \frac{|M^n|R}{J}. \tag{19}$$

Mesoscopic damage to soft rock tunnels occurs when $\sigma \geq \sigma_c$ or $\tau \geq \tau_c$, as shown in Fig. 2. The values of σ_c and τ_c determine the mechanical capacity of cementation, which can be obtained through a calibration process based on the peak strength of rock samples.

2.2.3 Creep-Induced Damage Phase Leading to Large Deformation

Clay minerals in soft rock may expand and disintegrate when exposed to water or constant loading. This long-term process can finally lead to the stress redistribution and damage accumulation of the rock surrounding the tunnel (Kontogianni et al. 2006; Tang et al. 2018; Xiong et al. 2020; Zhang et al. 2021). Because weak bonding is unable to carry tension, shear, and torsion, only the normal pressure is considered in the creep model. In this study, the creep behavior of soft rock is modeled using Burger's model, which combines the
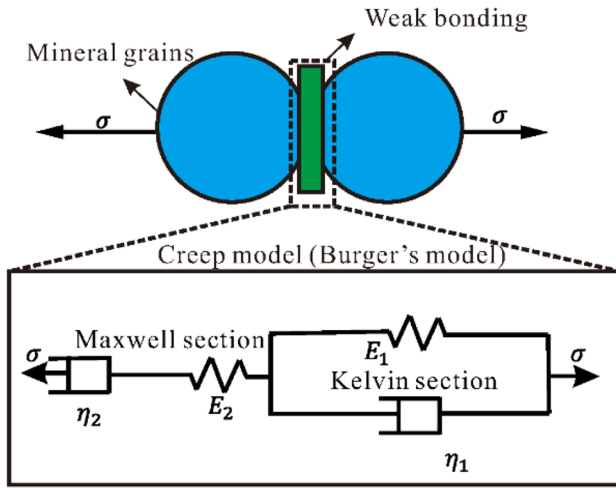
Fig. 4 Burger's creep model

Table 1 Governing equations of the Maxwell model, Kelvin model and Burger's model

Type of model	Governing equation (Maheshwari 2021)	Creep equation
Maxwell model	$\sigma = E_1 \varepsilon_k + \eta_1 \dot{\varepsilon}_k$	$\varepsilon = \frac{\sigma_0}{E_1}\left(1 - \exp\left(-\frac{E_1}{\eta_1} t\right)\right)$
Kelvin model	$\dot{\varepsilon}_M = \frac{\dot{\sigma}}{E_2} + \frac{\sigma}{\eta_2}$	$\varepsilon_M = \frac{1}{\eta_2}\sigma_0 t + \frac{\sigma_0}{E_2}$
Burger's model	$\ddot{\sigma} + \left(\frac{E_2}{\eta_1} + \frac{E_2}{\eta_2} + \frac{E_1}{\eta_1}\right)\dot{\sigma} + \frac{E_1}{\eta_1}\frac{E_2}{\eta_2}\sigma$ $= E_0\ddot{\varepsilon} + \frac{E_1 E_2}{\eta_1}\dot{\varepsilon}$	$\varepsilon = \frac{\sigma_0}{E_2} + \frac{\sigma}{\eta_2}t + \frac{\sigma_0}{E_1}\left(1 - e^{-\frac{E_1}{\eta_1}t}\right)$

characteristics of the Kelvin and Maxwell models (Fahimifar et al. 2010; Maheshwari 2021). Figure 4 shows the major components of Burger's model. The details are shown in Table 1.

Figure 5 shows the creep–damage model for simulating the large deformation and viscoelasticity damage of the soft rock surrounding the tunnel. It is assumed that the strong bonding is linear elastic before brittle failure, where E_3 is the linear elastic modulus.

The governing equations of Burger's model can be described as

$$\sigma + \alpha_1 \dot{\sigma} + \alpha_2 \ddot{\sigma} = \beta_1 \dot{\varepsilon} + \beta_2 \ddot{\varepsilon}, \tag{20}$$

where

$$\alpha_1 = \frac{\eta_1 + \eta_2}{E_1} + \frac{\eta_2}{E_2}, \tag{21a}$$

$$\alpha_2 = \frac{\eta_1 \eta_2}{E_1 E_2}, \tag{21b}$$

$$\beta_1 = \eta_2, \tag{21c}$$

$$\beta_2 = \frac{\eta_1 \eta_2}{E_1}. \tag{21d}$$

For a parallel connection, as shown in Fig. 5, the strain (ε_c) and stress (σ_c) of the coupled creep–damage model can be described as:

$$\varepsilon_c = \varepsilon = \varepsilon_3, \tag{22}$$

$$\sigma_c = \sigma_3 + \sigma, \tag{23}$$

$$\sigma_3 = E_3 \varepsilon_3. \tag{24}$$

where ε_3 and σ_3 are the strain and stress of the damage model. By combining Eqs. (20)–(24), the coupled creep–damage model can be derived as:

$$\sigma_c + \alpha_1 \dot{\sigma}_c + \alpha_2 \ddot{\sigma}_c = E_3 \varepsilon_3 + \left(\beta_1 + \alpha_1 E_3\right)\dot{\varepsilon}_3 + \left(\beta_2 + \alpha_2 E_3\right)\ddot{\varepsilon}_3. \tag{25}$$

At the initial phase ($t = 0, \sigma = \sigma_0$), Eq. (24) becomes

$$\ddot{\varepsilon}_c + \left(\frac{\beta_1 + \alpha_1 E_3}{\beta_2 + \alpha_2 E_3}\right)\dot{\varepsilon}_3 + \left(\frac{E_3}{\beta_2 + \alpha_2 E_3}\right)\varepsilon_c - \frac{\sigma_0}{\beta_2 + \alpha_2 E_3} = 0. \tag{26}$$

In addition, the initial conditions of strain, stress, and creep rate can be described as:

$$\varepsilon_c = \frac{\sigma}{E_1} = \frac{\sigma_3}{E_3}, \tag{27a}$$

$$\sigma_0 = \sigma_3 + \sigma, \tag{27b}$$

$$\varepsilon_c = \frac{\sigma_0}{E_1 + E_3}, \tag{28}$$

$$\dot{\varepsilon}_c = \frac{\sigma}{\eta_1} + \frac{\sigma}{\eta_2} = \frac{(\eta_1 + \eta_2)E_1 \sigma_0}{(E_1 + E_3)\eta_1 \eta_2}. \tag{29}$$

Equation (26) can be rewritten as

$$\ddot{\varepsilon}_c + A\dot{\varepsilon}_c + B\varepsilon_c = C, \tag{30}$$

where A, B and C are parameters related to the properties of the soft rock. By solving the second-order nonhomogeneous linear Eq. (30), the roots of the eigen-equation (i.e., λ_1 and λ_2) can be obtained as:

$$\lambda_{1,2} = \frac{A \pm \sqrt{A^2 - 4B}}{2} = \frac{-\left[\frac{(\eta_1 + \eta_2)E_1 E_3}{(E_1 + E_3)\eta_1 \eta_2} + \frac{E_1}{\eta_1}\right] \pm \sqrt{\left[\frac{(\eta_1 + \eta_2)E_1 E_3}{(E_1 + E_3)\eta_1 \eta_2}\right]^2 - 4\frac{E_1 E_2 E_3}{\eta_1 \eta_2 (E_1 + E_3)}}}{2}. \tag{31}$$

Then, the large deformation of the soft rock (ε_c) can be obtained as:

Fig. 5 Diagram of the creep–damage model
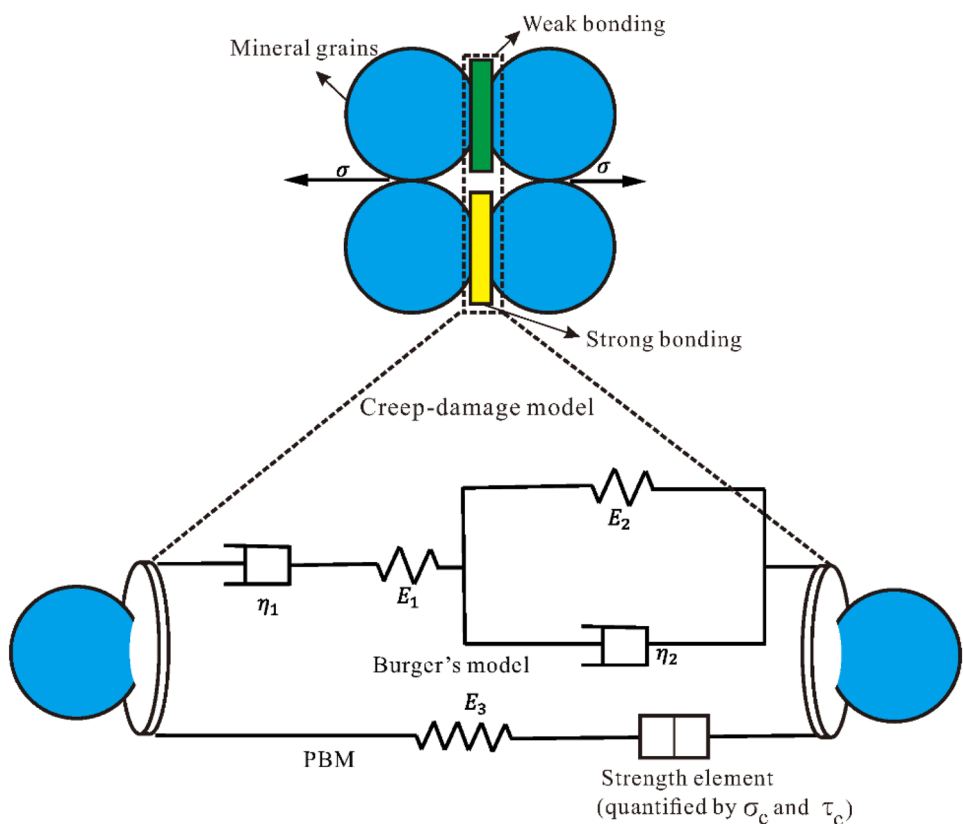
$$\varepsilon_c = C_1 e^{\lambda_1 t} + C_2 e^{\lambda_2 t} + \frac{\sigma_0}{E_3}. \tag{32}$$

The coefficients of C_1 and C_2 in Eq. (31) can be calculated when substituting Eqs. (27)–(29) into (30), and we obtain:

$$C_1 = \frac{(\eta_1 + \eta_2)E_1 E_3 \sigma_0 + \lambda_2 E_1 \eta_1 \eta_2 \sigma_0}{(\lambda_1 - \lambda_2)(E_1 + E_3)\eta_1 \eta_2 E_3}, \tag{33}$$

$$C_2 = \frac{(\eta_1 + \eta_2)E_1 E_3 \sigma_0 + \lambda_1 E_1 \eta_1 \eta_2 \sigma_0}{(\lambda_2 - \lambda_1)(E_1 + E_3)\eta_1 \eta_2 E_3}. \tag{34}$$

2.3 Coupled Meso/Macroscale Modeling of Damage and Deformation of the Surrounding Rock Resulting from Tunnel Excavation

The coupled meso/macroscale process resulting in the large deformation of soft rock can be described as:

$$d\varepsilon_{ij} = d\varepsilon_{ij}^e + d\varepsilon_{ij}^d + d\varepsilon_{ij}^{cd}, \tag{35}$$

where $\varepsilon_{ij}^e = D_{ijkl}\sigma_{ij}$, $d\varepsilon_{ij}^d = d\lambda \frac{\partial Q}{\partial \sigma_{ij}}$ and $d\varepsilon_{ij}^{cd} = \dot{\varepsilon}_c$. By considering the anisotropic mechanical behavior of the soft rock, Eq. (32) can be written as:

$$\varepsilon_{ij} = F(\sigma_{ij}, t), \tag{36}$$

where σ_{ij} represents the anisotropic mechanical behavior of the rock due to the tectonic stress condition at the macroscale. That is,

$$\sigma_{ij} = \begin{cases} \delta_{ij}\sigma_m + s_{kk}, \text{(non-hydrostatic state)} \\ \delta_{ij}\sigma_m, \text{(hydrostatic state)} \end{cases}. \tag{37}$$

Substituting Eq. (12) into Eq. (36), the multiscale coupled damage–creep model of soft rock surrounding a tunnel can be obtained,

$$\varepsilon_{ij} = F(\sigma_{ij} - \alpha_{kl}F_{ij}, t) + F'(\alpha_{kl}F_{ij}, t). \tag{38}$$

As shown in Fig. 6, Eq. (38) can be solved using the DEM based on a previously developed cell model that correlates the mesoscale structure and mechanical properties of soft rock (Li and Wong 2016; Xia et al. 2021a, b). The blue and green particles represent the normal and creep grains, respectively. It is assumed that there is a relatively strong bonding between the blue particles, whereas the bonding strength between green particles is relatively weak. The particles in the representative elementary volume (REV) are randomly arranged. In the numerical calculation, grain
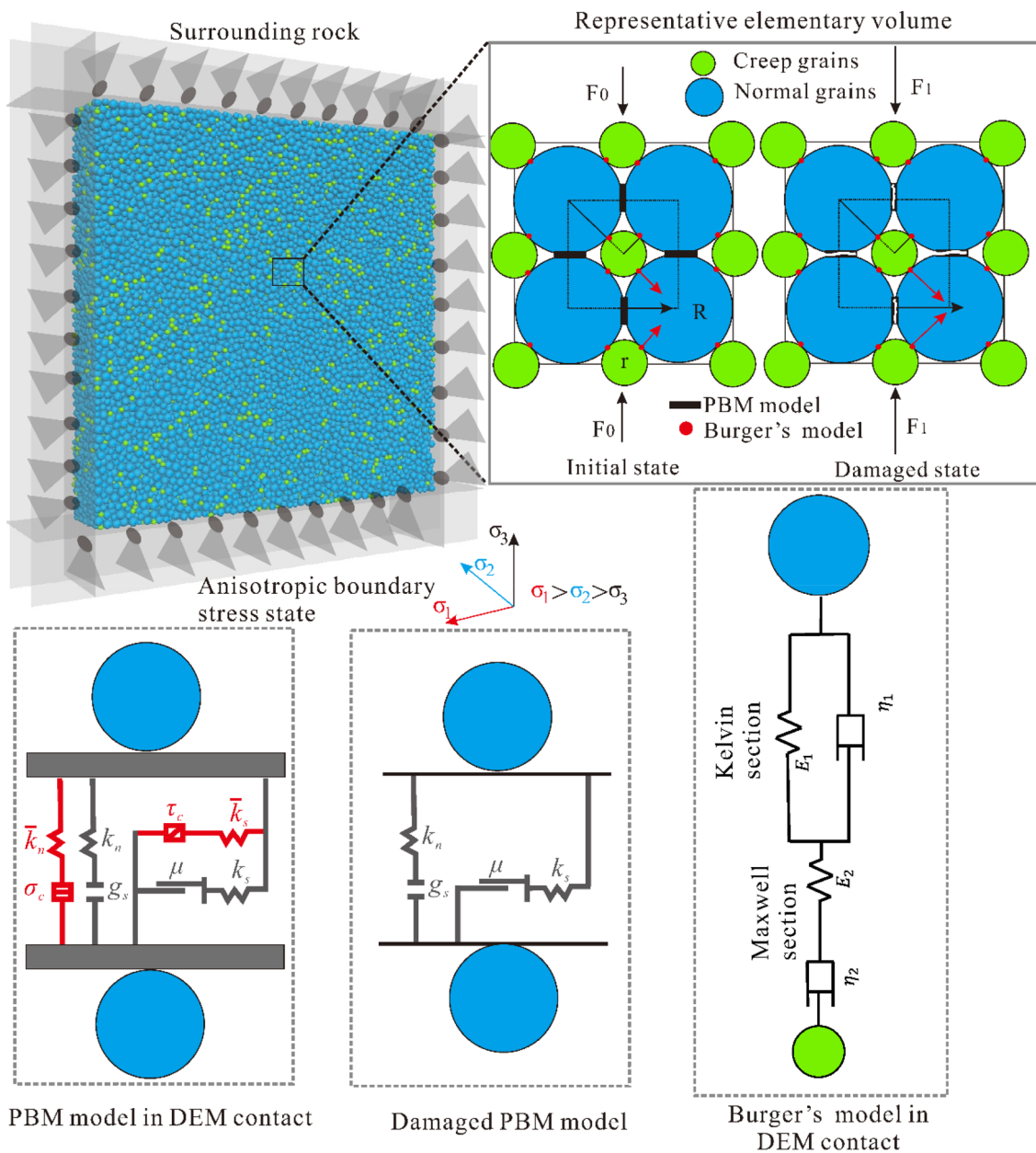
Fig. 6 Coupled meso/macroscale modeling using DEM

movement is determined by the model's boundary conditions and the mechanical evolution of bonding. Between two grains, the most common stress states are compressive or tensile forces applied to the normal direction of the bonding surface. The deformation between grains involves instantaneous and rheological deformation. The PBM mimicking strong bonding has five components (k_n, k_s, $\bar{k}_n$, $\bar{k}_s$ and σ_c). PBM deformation is determined by the normal (k_n, $\bar{k}_n$) and shear (k_s, $\bar{k}_s$) stiffnesses of springs. The damage is determined by the strength component σ_c, which complies with the threshold shown in Fig. 3. The Burger's model simulates

weak bonding by four components (E_1, E_2, η_1 and η_2). Weak bonding creep appears in the dashpot component (η_1, η_2) when a normal stress is applied. E_1 and E_2 are elastic springs herein.

2.4 Modeling of the Long-Term Deformation of a Tunnel

2.4.1 Project Description

The soft rock tunnel selected in this study is located in northwest China with a total length of approximately 15 km and a

Fig. 7 Tunnel faces showing the soft rock surrounding the tunnel and bedding joints. **a** Deformation of the tunnel surrounding rock in the left corner, **b** deformation of the left tunnel surrounding rock (Zhang et al. 2020), **c** BLSS 3D laser scanner used in rock mass deformation monitoring, and **d** Leica TCA2003 Total Station used for monitoring displacement of three points
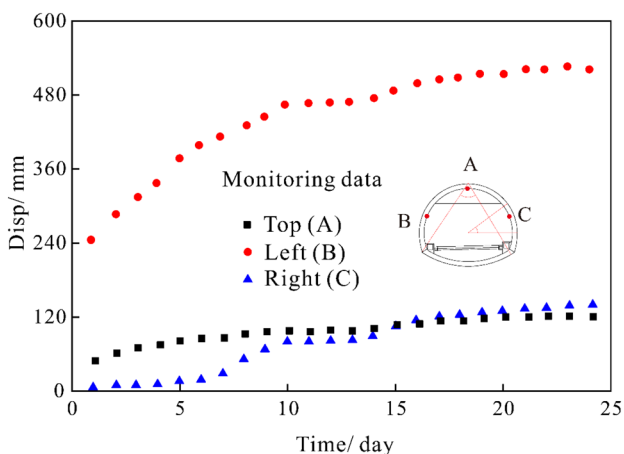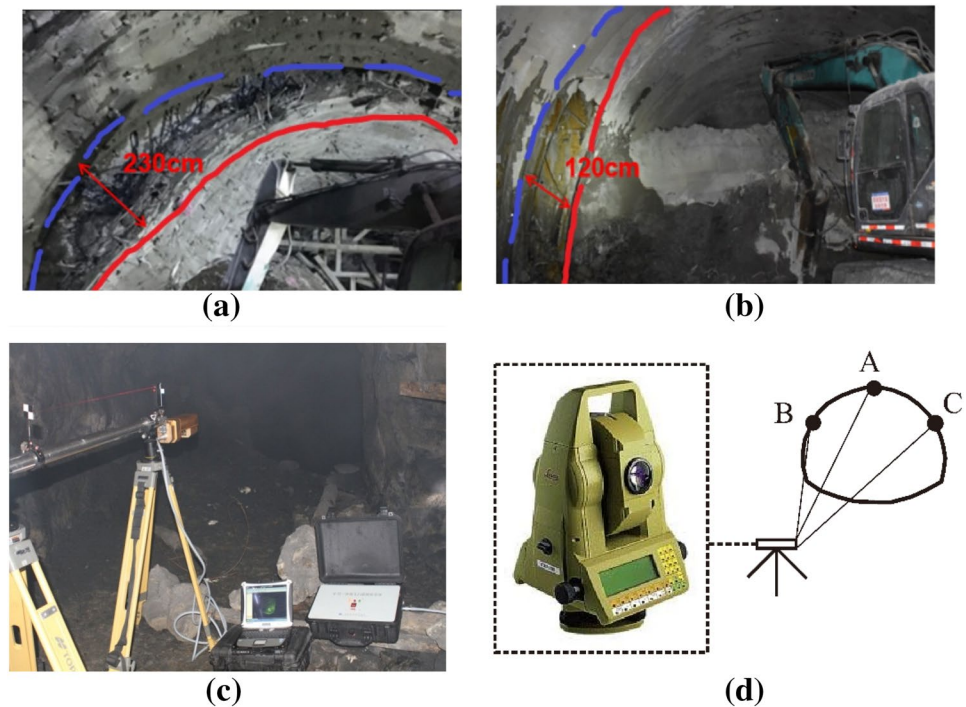

Fig. 8 Time-dependent displacement at monitoring points "*A*", "*B*" and "*C*" in tunnel section "XK0＋060−XK0＋250"

maximum buried depth of 638 m (Chen et al. 2020; Zhang et al. 2020; Sun et al. 2021; Liu et al. 2022). Due to the instability of soft rock with a uniaxial saturated compressive strength of less than 30 MPa, collapses often occur. The tunnel faces show the soft rock surrounding the tunnel and bedding joints (Fig. 7) (Zhang et al. 2020). The inclination angle of the main joints of the surrounding rock is approximately 30°–85°, while the thickness between the joint surfaces is approximately 5–30 cm. Based on the X-ray diffraction tests, the main mineral components of the rock are clay and

quartz. The average uniaxial strength of the rock samples is 29.6 MPa, while the average strength under water saturation for 24 h is 12.7 MPa. In addition, the tectonic stress measured by the original hydraulic fracturing shows that the maximum and minimum horizontal principal stresses are 20 and 14 MPa, respectively (Zhang et al. 2020). The deformation of the surrounding soft rock after excavation is relatively large, with the convergent deformation exceeding 1 m.

A total station and 3D laser scanner were used to monitor the section of the No. 2 inclined shaft of the tunnel. The deformation of the surrounding rock mass was measured by a BLSS 3D laser scanner. The 3D spatial deformation was calculated by distance, angle, and inclination correction, which was recorded by a laser distance sensor, position feedback encoder and inclination sensor, respectively. The measuring accuracy of the BLSS 3D laser scanner is 0.7 mm in a 10-m range. The final deformation is shown in Fig. 7a, b.

The monitored displacement of points "*A*", "*B*", and "*C*" was measured by a Leica TCA2003 total station. When measuring, the reference point is set up at a stable place, and reflective sheet targets are attached to the top of the vault. Three measurements were taken at each point for the average, which was continuously monitored for 25 days during the excavation. The monitoring results of the tunnel section investigated are presented in Fig. 8. The measuring range and accuracy of the Leica TCA2003 total station are 1000 and 0.1 mm, respectively.
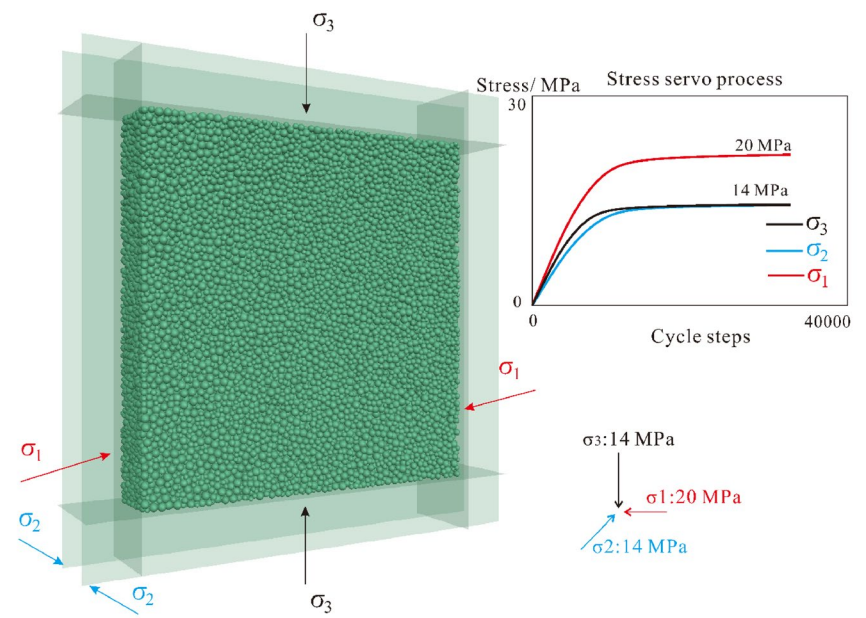
(a) Defining the simulation domain. "A", "B" and "C" are three monitoring points
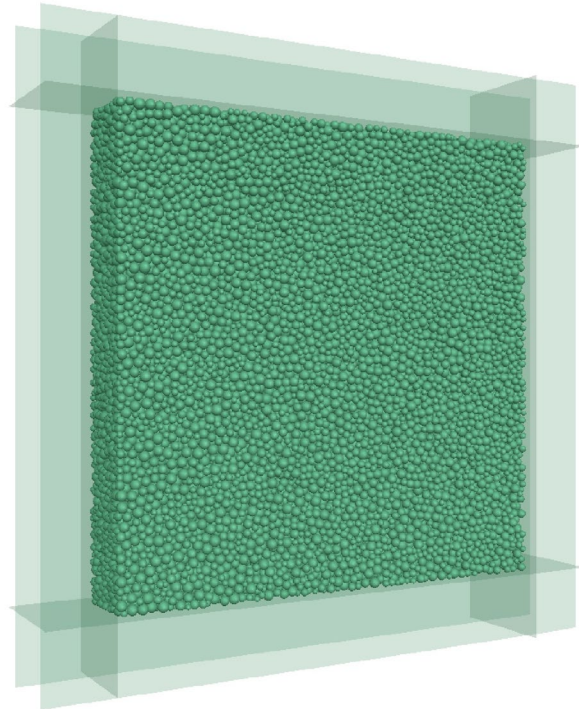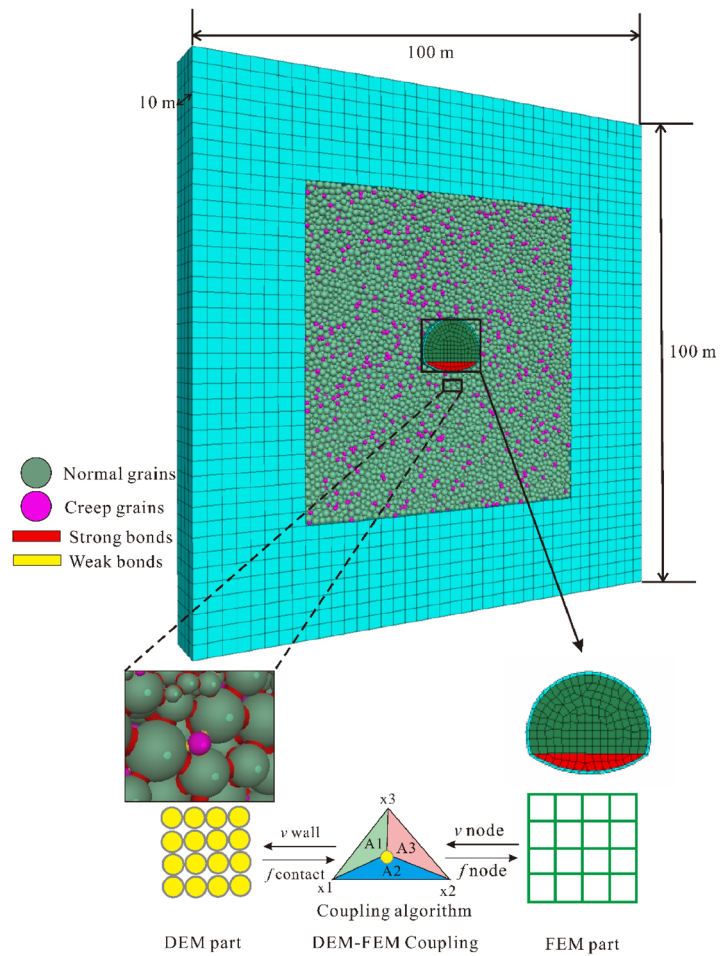

(b) Distribution of grain particles within the simulation domain
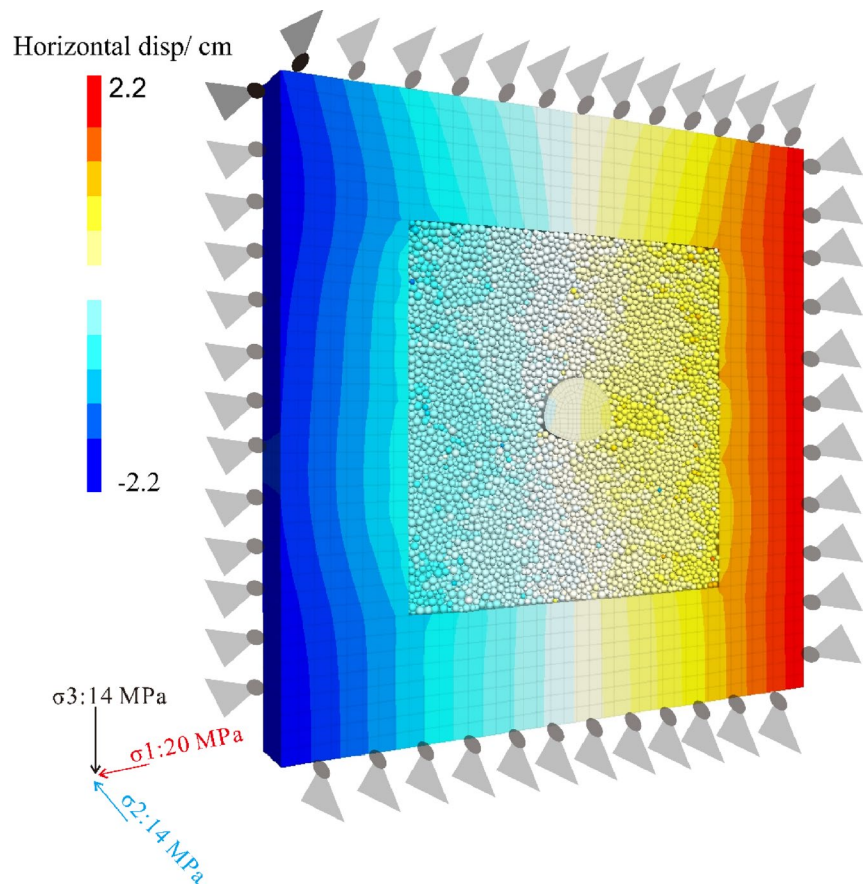
Fig. 9 (continued)

(c) Tectonic stresses applied to the domain

(d) Combined finite and discrete element approach

Fig. 9 (continued)

(e) Initial joints applied to the tunnel surrounding rock

2.4.2 Model Setup and Calibration

The numerical modeling process involves the following five steps:

(1) Define the simulation domain of the grain model

As shown in Fig. 9a, the size of the research domain is 60 m (width) × 60 m (height) × 10 m (length), considering the size of the tunnel. "*A*", "*B*", and "*C*" are the three monitoring points in the tunnel face.

(B) Distribute the grain particles into the simulation domain

As shown in Fig. 9b, the grains are uniformly distributed between the boundaries of the domain, and the mechanical system is iterated until equilibrium is reached, in which fine particles are distributed in the tunnel zone (Gutierrez-Ch et al. 2022). Considering the modeling convenience, the fine particle zone is selected in a square region. The density and modulus of the grain assembly are

2500 kg/m^3 and 600 MPa, respectively, based on the rock samples obtained from the tunnel.

(C) Tectonic stresses applied to the domain

As shown in Fig. 9c, the tectonic stresses according to the in situ stress condition are applied to the simulation domain based on the servo method (Lin et al. 2022). The stress is calculated based on the overall contact force between grains and walls, while the velocity of walls is controlled by FISh (a computer coding language commonly used for DEM) until the dynamic stress balance is reached. The in situ stress is determined based on the field measurement results, i.e., the maximum, intermediate and minimum principal stresses are 20, 14 and 14 MPa, respectively.

(D) Combined finite and discrete element approach

In the numerical simulation, the model length is usually set to nearly eight times the tunnel diameter to avoid boundary effects. However, limited by computing efficiency, the DEM grain-based model cannot meet all the requirements.

Thus, as shown in Fig. 9d, a combined DEM–FEM approach (Huang et al. 2020a, b; Wang et al. 2020) was used in this paper for modeling the continuous deformation in the inner zone and expanding the simulation range. The inner FEM zone is used for the support material. In the DEM–FEM coupled zone, the calculated unbalanced force of grains will be attributed to the adjacent FEM nodes. This will cause a velocity alteration of FEM nodes, which will be assigned to the adjacent grains. The above coupling process is completed in each timestep. Before the model implementation, bonding models were added, and it is assumed that the cemented grains form a stable system. The bonding strength between the grain particles was calibrated based on the average strength of the intact rock mass (i.e., approximately 30 MPa). It is important to note that the already existing rock support could influence the initial equilibrium. After excavation, the support element was applied with a null modulus. The real lining structure is installed instantly after Day 1 when creep deformation begins.

(E) Application of initial joints and boundary conditions

As shown in Fig. 9e, the deformation due to excavation can be modeled using the commercial DEM software Particle Flow Code (PFC). The modeling process of the joints is realized by using the smooth joint model in PFC, which can provide relative sliding friction (Hu et al. 2018). After the application of joints, the initial equilibrium before excavation was obtained under the boundary conditions shown in Fig. 9e. After excavation, the displacements at monitoring points "A", "B" and "C" were numerically predicted.

When a mesoscale modeling approach is used to model the mechanical response of rocks, the mechanical parameters of grain elements as well as bonding elements need to be well calibrated (see Fig. 10). In this paper, the calibration process is complex for considering joints and creep conditions. Typically, the strength and elastic modulus of

Table 2 Mechanical and physical properties used in mesoscopic scale analysis

	Value
Parameters used in PBM group	
PBM tensile strength (MPa)	30
PBM cohesive strength (MPa)	62
PBM effective modulus (GPa)	7.6
Normal stiffness of PBM group (N/m)	8.44×10^9
PBM friction (°)	20
Ratio of normal to shear stiffness of PBM	1.2
Grain normal stiffness (N/m)	8.44×10^9
Ratio of normal to shear stiffness of grains	1.2
Grains friction coefficient	0.57
Density of grains (kg/m³)	2500
Grain number	31,516
Damping coefficient	0.5
Parameters used in Burger's group	
Stiffness of Kelvin section (N/m)	1.1×10^9
Stiffness of Maxwell section (N/m)	1.1×10^9
Viscosity of Kelvin section (N•s/m)	1.2×10^8
Viscosity of Maxwell section (N•s/m)	1.3×10^6
Parameters used in smooth joints group	
Normal stiffness per unit area of the smooth joint model (N/m³)	1.5×10^9
Shear stiffness per unit area of the smooth joint model (N/m³)	1.5×10^9
Friction coefficient of the smooth joint model	0.07
Tensile strength of smooth joints model (MPa)	1.2
Cohesive strength of smooth joints model (MPa)	2.4
Parameters used in FEM analysis	
Poisson ratio	0.25
Density (kg/m³)	2500
Modulus (GPa)	0.6

rock are determined by a 'trial and error' process (Coetzee 2017). In this paper, we calibrate the creep, strength, and

Fig. 10 Numerical parameters need to be determined at different modeling scales and scenarios, including (1) static mechanical property and creep property calibration in rock samples; (2) verification of the calibrated model at the engineering scale; and (3) back-analysis for obtaining the mechanical properties of joints
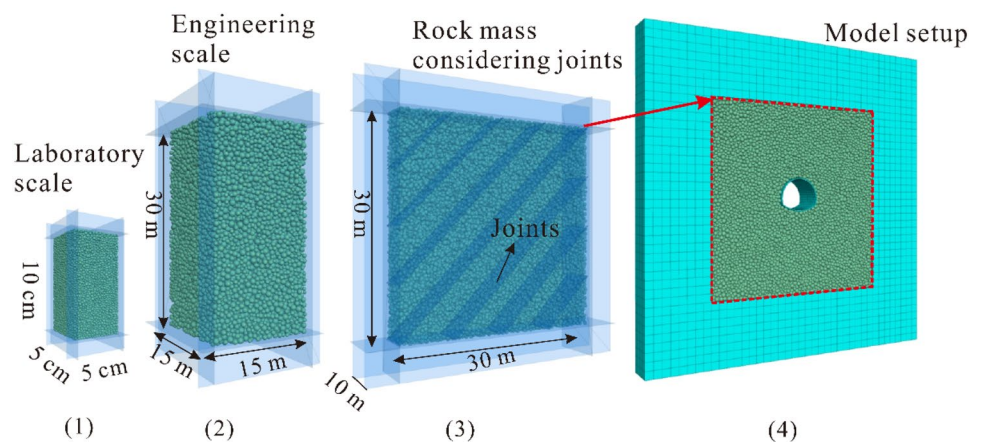
joint parameters in the order shown in Fig. 10, which is presented in Table 2. The trials involved were repeated three times under different random seeds.

Based on field investigation, the basic rock properties are obtained from (Zhang et al. 2020), and the time-dependent creep test results are collected from (Tao et al. 2020). The mesoscale parameters presented in Table 2 are determined according to the following steps:

(1) General parameters adopted in the DEM modeling

In the grain-based model, we need to consider calculation accuracy and efficiency. According to a previous study, when *L/R* (where *L* is the model length and *R* is the mean grain radius) is greater than 68, the properties of the material are

Table 3 Mechanical properties of the rock sample in the calibrated and experimental results

	Young's modulus (MPa)	UCS (MPa)	Cohesion strength (MPa)	Friction angle (°)
Experiments	7.60	29.60	8.6	29
Calibrations	7.55	29.64	8.7	28.7
Error	0.66%	0.13%	1.1%	1.0%

nearly constant (Li et al. 2014; Cheng and Wong 2020). Previous studies have shown that in a DEM system, the number of mesoscale elements can meet the requirements of accuracy and calculation efficiency when greater than 15,000

Fig. 11 Calibration results. **a** Uniaxial loading stress–strain curves of intact rock samples, **b**, **c** strain curves of creep test, **d** uniaxial loading stress–strain curves of intact rock mass, and **e** uniaxial loading stress–strain curves of jointed rock mass
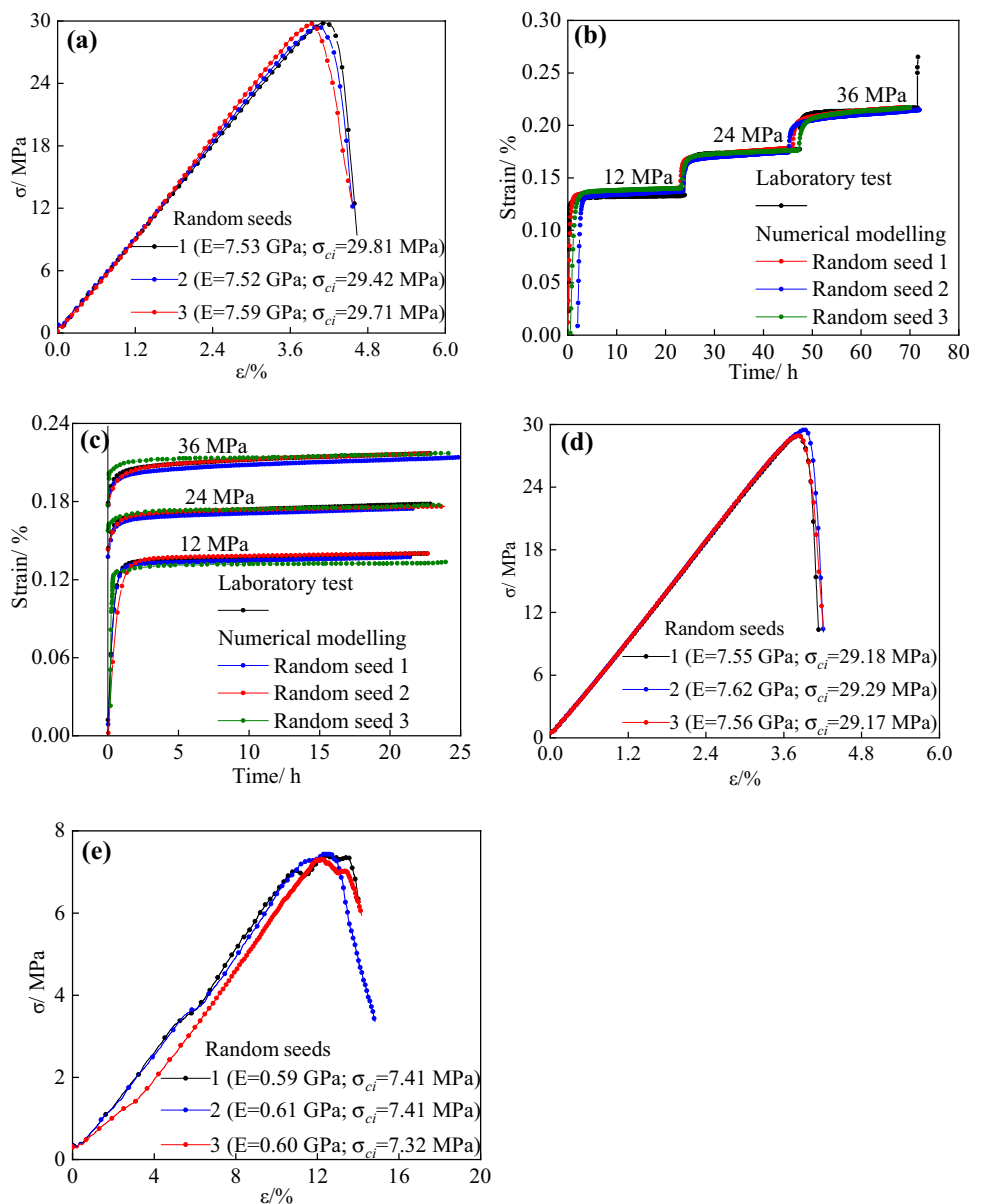
(Lin et al. 2022). In the rock sample and rock mass calibration, we choose an L/R value greater than 100 in this paper. A total of 31,516 grains were used in the simulation based on convergence analysis. The damping coefficient is set to a default value of 0.5 to dissipate kinetic energy.

(B) Loading test calibration

Static mechanical properties were calibrated prior to the creep deformation parameters. The loading test is the most commonly adopted method to characterize the elastic modulus and strength of rock samples. We conducted numerical tests to obtain reasonable bonding strength and stiffness. The calibration results are shown in Fig. 11a, where we find that the mechanical properties are well-calibrated compared to the real rock parameters. We compared the detailed mechanical properties of the rock samples in Table 3.

(C) Creep test calibration

Because of the rheological deforming scenario discussed in this paper, we need to consider two kinds of contacts as bonding. The ratio of PBM to Burger's model and their parameters will affect the final creep behavior of the rock. In this stage, the bonding strength is applied to a high value (tensile strength = 200 MPa, cohesive strength = 400 MPa), which will not damage the creep tests. The calibration process is finished by changing the parameter values after the 'trial and error' process.

Table 4 Creep deformation under different normal stresses

	Strain (%)	Error (%)
12 MPa stage		
Lab result	0.1336	
Seed 1	0.1409	5.5
Seed 2	0.1374	2.8
Seed 3	0.1401	4.8
		4.3 (mean error)
24 MPa stage		
Lab result	0.1773	
Seed 1	0.1782	0.5
Seed 2	0.1746	1.5
Seed 3	0.1762	0.6
		0.87 (mean error)
36 MPa stage		
Lab result	0.2160	
Seed 1	0.2170	0.45
Seed 2	0.2147	0.6
Seed 3	0.2172	0.46
		0.5 (mean error)

The creep tests were carried out at 12, 24 and 36 MPa stresses (see Fig. 11). During the creep simulation process, we found that the results were reasonable when equating 5×10^5 steps to a real 24 h in the laboratory. We keep the same treatment in this paper in regard to the conversion of timesteps to real time. In the calibrated sample, creep grains make up 18.7% of the total grains, which are randomly distributed in the particle assemblage. The final calibration results are presented in Fig. 11b, c, where we can compare the creep curves. The detailed calibration error is shown in Table 4, and the mean error of creep strain in different loading forces is less than 5%.

(D) Verification on the engineering scale

According to the mentioned conclusion, when the model size to grain size ratio is larger than 68, the mechanical behavior of the DEM model is constant. It is necessary to verify this conclusion to promote mesoscale parameters to an engineering scale. Therefore, we conducted an engineering scale (15 m × 15 m × 30 m) uniaxial loading test via the DEM. We find that when the model size to grain size ratio is fixed, the strength and elastic modulus of the rock are also nearly constant (see Fig. 11d).

(E) Bedding joint parameter calibration for rock mass

After rock sample calibration, we need to further determine the rock mass properties, where the joints are considered. Numerical back-analysis is a powerful method that can be used as a complementary technique to in situ or laboratory experiments to determine mechanical properties (Fakhimi et al. 2004; Li et al. 2022a, b). In situ failure, movement or convergence can be used to back-calculate the physical properties of rock joints. In this paper, the following steps were used for back-analysis:

A. Strength of 29.6 MPa and elastic modulus of 7.6 GPa were used as determined from the laboratory loading test.
B. A joint angle of 45 ° and a spacing of 15 m were assumed. The value of angle and space was justified based on field mapping.
C. Reasonable values for joint roughness, joint cohesive strength, and friction coefficients based on the results of in situ tests and engineering judgment were assumed. We modified these parameters until there was good agreement between the numerical and measured in situ failures. After the back-analysis process, we obtained a reasonable rock mass numerical mechanical property compared with the rock mass property ($E = 0.6$ GPa, σ_{ci}=7.4 MPa) obtained from field investigation (Zhang et al. 2020).

Fig. 13 The ultimate displacements at points "*A*", "*B*" and "*C*" with or without initial joints
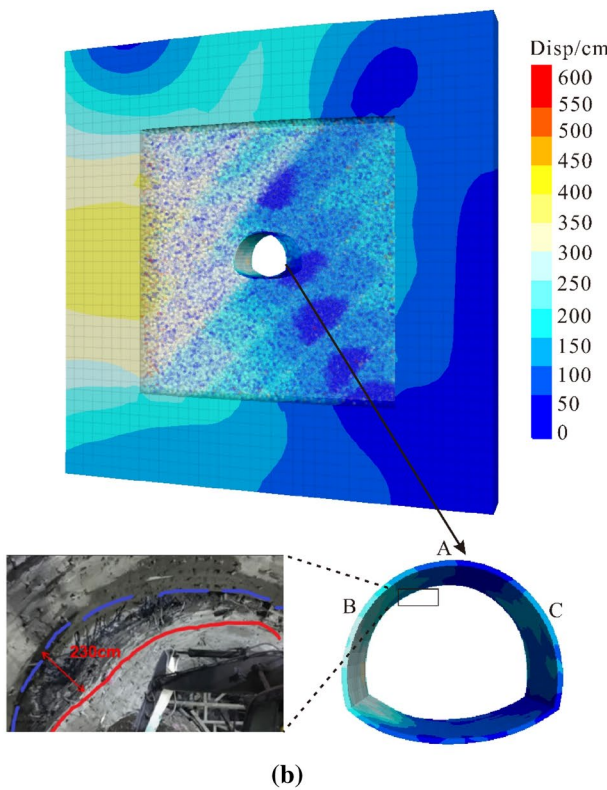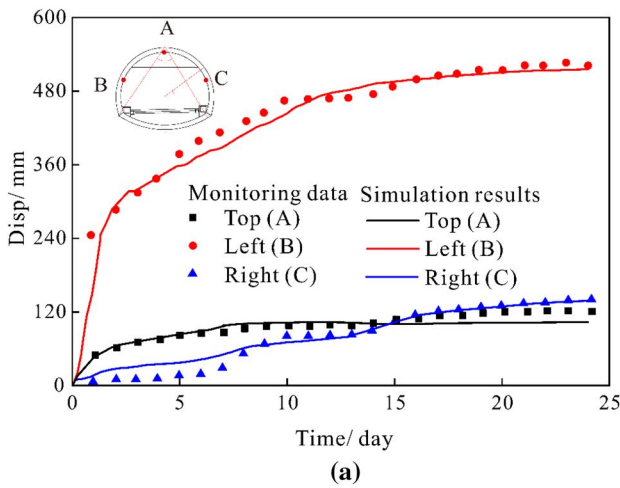

Fig. 12 Macroscopic deformation of the soft rock surrounding the tunnel during the excavation: **a** comparing the predicted time-dependent displacements at "*A*", "*B*" and "*C*" with monitoring data, **b** displacement contour in the simulation domain and observed tunnel surface extrusion in the field

3 Results and Discussion

3.1 Comparison Between the Predicted Displacement and Monitoring Data

Figure 12 shows the macroscopic deformation of the

surrounding rock during the excavation. It shows that the predicted time-dependent displacements at "*A*", "*B*" and "*C*" agree with the monitoring data reasonably well. In addition, the displacement at point "*B*" is larger than that at "*A*" and "*C*". For example, on Day 25 after the excavation, the displacement at point "*B*" is more than twofold larger than that at point "*C*". Furthermore, the maximum displacement surrounding the surface of the tunnel is approximately 526 mm, which could lead to tunnel damage.

3.2 The Asymmetrical Deformation of the Tunnel Face at Monitoring Points "*B*" and "*C*"

The deformation of the rocks surrounding the tunnel face is generally asymmetric due to the application of joints with different inclination angles (i.e., 30°, 45°, and 60°), and the asymmetric nature of the deformation becomes obvious at a joint inclination angle of 45° (Zhang et al. 2020). As shown in Fig. 13, the deformations at points "*B*" and "*C*" are symmetrical without initial joints, whereas the application of initial joints could lead to a significant difference in displacement between "*B*" and "*C*". Under the joint inclination angle of 45°, the rock mass is prone to slide along the joint surface, which ultimately could lead to a large displacement on the left side of the tunnel.

Figure 14 demonstrates the movement of rock grains, which is captured from the initial equilibrium stage at cycle time step 10,000. The movement of rock grains demonstrates a symmetrical "X" shape, whereas the application of initial joints could result in the location of grains along the joints and two shearing zones. As monitoring point "*B*" is in one of the shearing zones, it has the largest displacement among the three measuring points.

Fig. 14 Movement of grains with or without initial joints

(a)   (b)
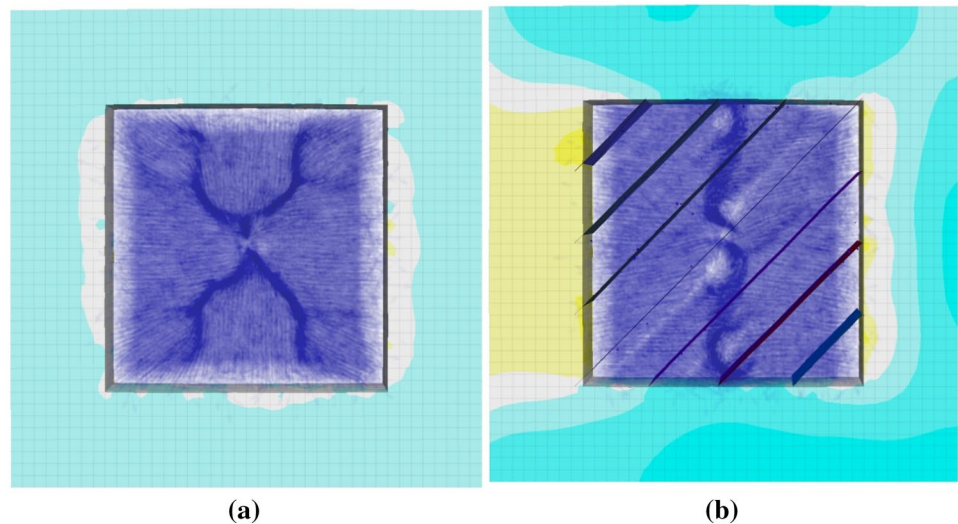
3.3 Mesoscopic Scale Damage and Deformation of the Surrounding Rock at Different Phases

As shown in Fig. 15, the large deformation of soft rock surrounding the tunnel is a gradual process. In the initial phase, the whole surrounding rock is stable. Due to the excavation-induced stress redistribution, the surrounding rock undergoes the loading phase, in which the weak bonds in the rock experience creep under excessive local stresses. As the deformation accumulates, creep-induced damage develops around the tunnel. The coupled creep–damage process ultimately causes large deformation of the surrounding rock of the tunnel. From Days 1–4, the excavation-caused stress concentration around the tunnel causes severe mesocrack accumulation; the creep-induced stable increase in crack number is captured thereafter.

3.4 Model Sensitivity Analysis

Given the complexity of the scenario considered in this paper, we conducted a sensitivity analysis of the proposed model.

(1) Effect of the change in tensile/cohesive strength on the final displacement

Figure 16 shows the predicted ultimate displacement at points "*A*", "*B*" and "*C*" under different bonding strengths of cementations quantified by the mesoscopic tensile and cohesive strength of the rock grains. The initial values of the bonding characteristics (σ_c =30 MPa, τ_c = 61 MPa) are obtained through the calibration process based on the peak strength of the rock samples. It shows that the decrease of the bonding tensile strength by 50% could increase the displacement at the top of the tunnel (point "*A*") by 300% but have relatively little influence on the displacements at points "*B*" and "*C*". However, the same proportional change in cohesive strength has a smaller effect on the final deformation. Thus, the final deformation is more sensitive to the tensile strength.

(B) Effect of the fraction of grains experiencing creep on the model mechanical responses

In this paper, we have coupled the damage and creep factors in a soft rock tunnel, and we also obtained a reasonable result. We refer to the grains that undergo creep as creep grains. We extended our discussion to some more scenarios with different creep grain ratios involving 18.7, 20.2, 21.7, 23.2 and 24.7% (Fig. 17). The rock strength, creep strain, and excavation deformation at three monitoring points "*A*" "*B*" and "*C*" are compared in Table 5 and Fig. 18 for sensitivity analysis. When the creep grain ratio rises to 24.7%, the error of the predicted deformation at the three monitoring points becomes large (greater than 10%). If this ratio continues to increase, the deformation prediction results obtained will differ significantly from the actual situation.

In a time-dependent comparison, we conducted creep tests for laboratory-scale rock samples under 24 MPa stress. Figure 17 shows that the ultimate creep strain and deformation at the left side of tunnel monitor point "*B*" increase with increasing creep grain ratio. When the incremental creep grain ratio increases from 4.5 to 6.0%, the incremental deformation at the three monitoring points nearly doubles.

Fig. 15 The soft rock tunnel surrounding rock at different phases: **a** deformation maps and damage zones captured on different days, **b** counted crack numbers in the modeling process
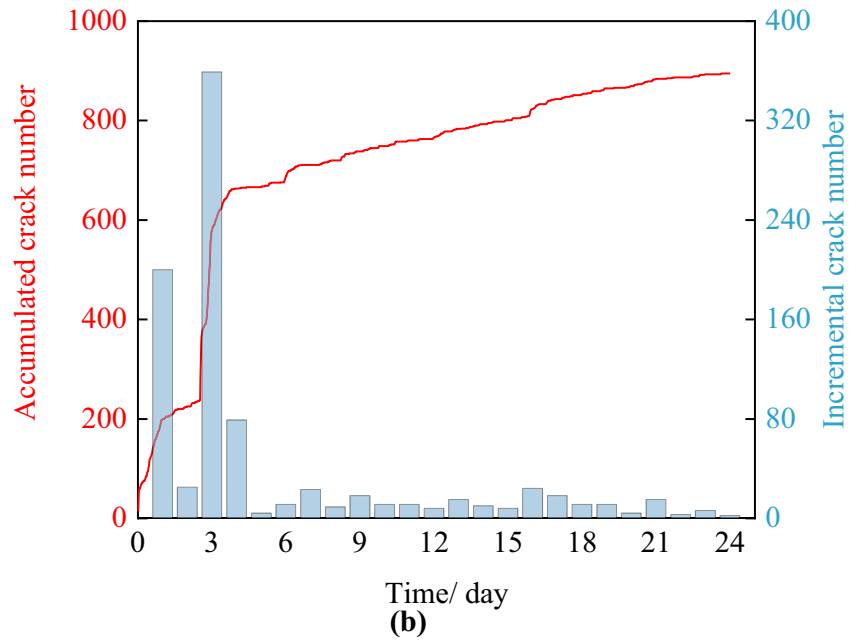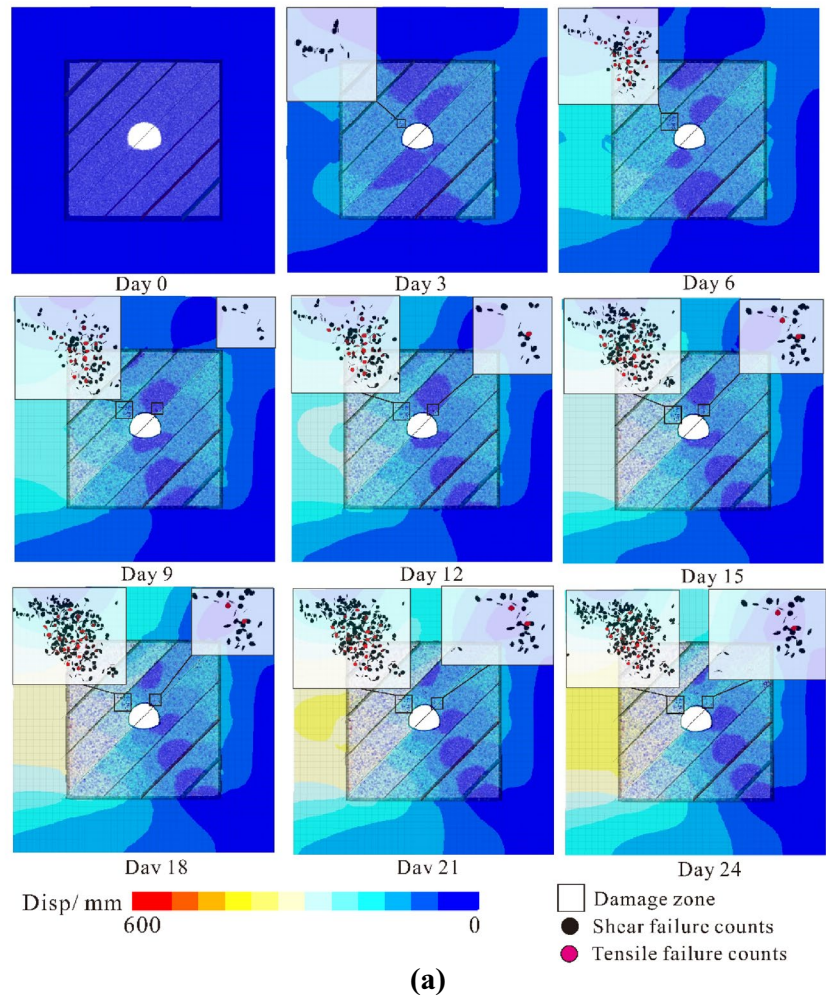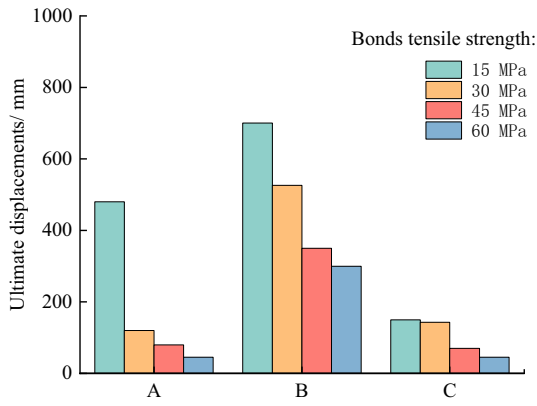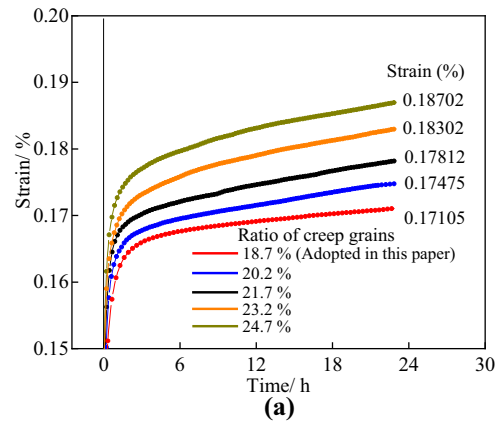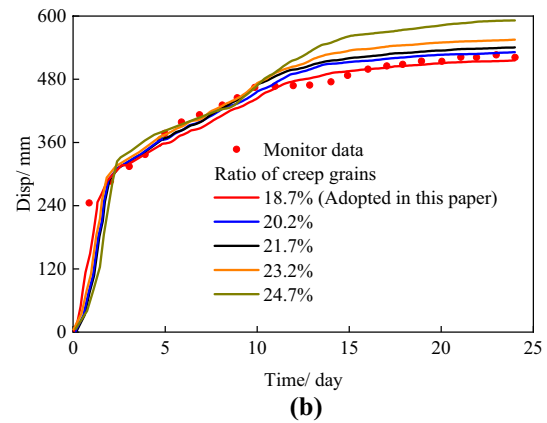

(a)
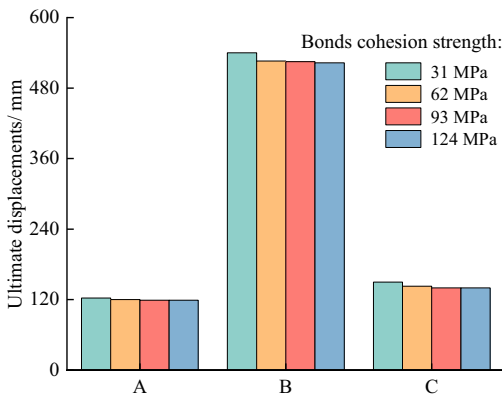
(b)

Fig. 16 The predicted displacement at points "*A*", "*B*" and "*C*" under different bonding strengths: **a** change in bond tensile strength and **b** change in bond cohesive strength

Fig. 17 Time-dependent behavior under different ratios of creep grains: **a** creep curves of the rock sample under 24 MPa loading and **b** rheological displacement at the left point "*B*" of the tunnel

4 Conclusions

We implemented a damage-based, time-dependent modeling approach to reproduce the entire evolution of a large-deformation soft rock tunnel. By incorporating the coupled meso/macroscale deformation process of the rock into the model, the predicted time-dependent displacements of the tunnel face agree reasonably well with the monitoring data.

Table 5 The influence of changing the creep grain ratio on the modeling results

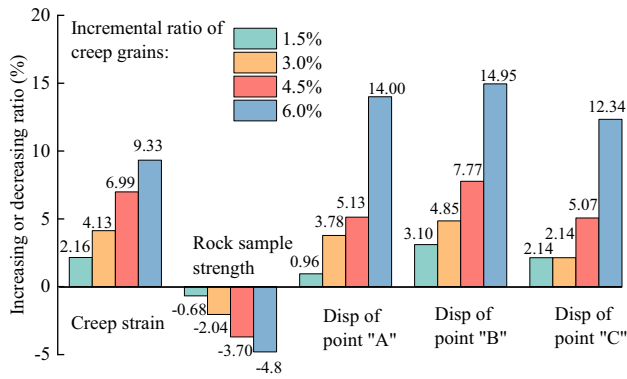| Creep grains ratio (%)	Strain of creep test (%)	Rock strength (MPa)	Ultimate displacement at "A" (mm)	Ultimate displacement at "B" (mm)	Ultimate displacement at "C" (mm)
18.7	0.17105	29.4	103.3	525.9	140.1
20.2	0.17475	29.2	104.3	531.4	143.0
21.7	0.17812	28.8	107.2	540.5	143.1
23.2	0.18302	28.3	108.6	555.2	147.2
24.7	0.18702	27.9	128.7	592.0	157.4

Fig. 18 Comparison of the influence of changing the creep grain ratio on different modeling results

The model is able to reproduce both instantaneous damage patterns of brittle failure and time-delayed creep deforming patterns. Tunnel excavation strongly affects the initial stability of the surrounding rock mass, and brittle damage accumulated in mineral clusters leads to severe instantaneous deformation, which becomes less important in the creep evolution stage.

The application of the theoretical model to engineering cases provided the opportunity to investigate the evolution mechanisms of large deformation. As an emerging property, the model simulates a wider range of scenarios with different rock static and creep parameters. The final deformation is characterized by a high sensitivity to the value of mesoscale modeling parameters.

Data availability The authors confirm that the data supporting the findings of this study are available within the article.

Declarations

Conflict of interest The authors declare that they have no conflicts of interest related to this work.

References

Bahaaddini M, Sharrock G, Hebblewhite BK (2013) Numerical direct shear tests to model the shear behaviour of rock joints. Comput Geotech 51:101–115

Chen J, Liu W, Chen L, Luo Y, Li Y, Gao H, Zhong D (2020) Failure mechanisms and modes of tunnels in monoclinic and soft-hard interbedded rocks: a case study. KSCE J Civ Eng 24(4):1357–1373

Cheng Y, Wong LNY (2020) A study on mechanical properties and fracturing behavior of Carrara marble with the flat-jointed model. Int J Numer Anal Methods Geomech 44(6):803–822

Coetzee CJ (2017) Calibration of the discrete element method. Powder Technol 310:104–142

Cui Z, Sheng Q, Leng X, Ma Y (2019) Investigation of the long-term strength of Jinping marble rocks with experimental and numerical approaches. Bull Eng Geol Environ 78(2):877–882

Cui G, Zhou C, Liu Z, Xia C, Zhang L (2022) The synthesis of soft rocks based on physical and mechanical properties of red mudstone. Int J Rock Mech Min Sci 151

Deng XF, Zhu JB, Chen SG, Zhao ZY, Zhou YX, Zhao J (2014) Numerical study on tunnel damage subject to blast-induced shock wave in jointed rock masses. Tunn Undergr Space Technol 43:88–100

Fahimifar A, Tehrani FM, Hedayat A, Vakilzadeh A (2010) Analytical solution for the excavation of circular tunnels in a visco-elastic Burger's material under hydrostatic stress field. Tunn Undergr Space Technol 25(4):297–304

Fakhimi A, Salehi D, Mojtabai N (2004) Numerical back analysis for estimation of soil parameters in the Resalat Tunnel project. Tunn Undergr Space Technol 19(1):57–67

Guo W-B, Hu B, Cheng J-L, Wang B-F (2020) Modeling time-dependent behavior of hard sandstone using the DEM method. Geomech Eng 20(6):517–525

Gutierrez-Ch JG, Senent S, Zeng P, Jimenez R (2022) DEM simulation of rock creep in tunnels using rate process theory. Comput Geotech 142

Hu W, Kwok CY, Duan K, Wang T (2018) Parametric study of the smooth-joint contact model on the mechanical behavior of jointed rock. Int J Numer Anal Methods Geomech 42(2):358–376

Huang F, Wu C, Jang B-A, Hong Y, Guo N, Guo W (2020a) Instability mechanism of shallow tunnel in soft rock subjected to surcharge loads. Tunn Undergr Space Technol 99

Huang M, Zhan JW, Xu CS, Jiang S (2020b). New creep constitutive model for soft rocks and its application in the prediction of time-dependent deformation in tunnels. Int J Geomech 20(7)

Jia P, Tang CA (2008) Numerical study on failure mechanism of tunnel in jointed rock mass. Tunn Undergr Space Technol 23(5):500–507

Jiang J, Liu Q, Xu J (2016) Analytical investigation for stress measurement with the rheological stress recovery method in deep soft rock. Int J Min Sci Technol 26(6):1003–1009

Kabwe E, Karakus M, Chanda EK (2020a) Creep constitutive model considering the overstress theory with an associative viscoplastic flow rule. Comput Geotech 124

Kabwe E, Karakus M, Chanda EK (2020b) Isotropic damage constitutive model for time-dependent behaviour of tunnels in squeezing ground. Comput Geotech 127

Kontogianni V, Psimoulis P, Stiros S (2006) What is the contribution of time-dependent deformation in tunnel convergence? Eng Geol 82(4):264–267

Kovacevic MS, Bacic M, Gavin K, Stipanovic I (2021). Assessment of long-term deformation of a tunnel in soft rock by utilizing

particle swarm optimized neural network. Tunn Undergr Space Technol 110

Li G, Tang C-A (2015) A statistical meso-damage mechanical method for modeling trans-scale progressive failure process of rock. Int J Rock Mech Min Sci 74:133–150

Li B, Wong RCK (2016) Quantifying structural states of soft mudrocks. J Geophys Res-Solid Earth 121(5):3324–3347

Li B, Guo L, Zhang F-S (2014) Macro-micro investigation of granular materials in torsional shear test. J Cent South Univ 21(7):2950–2961

Li W, Han Y, Wang T, Ma J (2017) DEM micromechanical modeling and laboratory experiment on creep behavior of salt rock. J Nat Gas Sci Eng 46:38–46

Li H, Eshiet KII, Sheng Y, Zhong ZL, Liu XR, Yang DM (2018) A parallel-bonded chemical corrosion model for discrete element modelling of chemically corroded limestone. Eng Fract Mech 202:297–310

Li X, Si G, Oh J, Canbulat I, Xiang Z, Li T (2022a) A pre-peak elastoplastic damage model of Gosford sandstone based on acoustic emission and ultrasonic wave measurement. Rock Mech Rock Eng 55(8):4819–4838

Li X, Si G, Oh J, Corbett P, Xiang Z, Aziz N, Mirzaghorbanali A (2022b) Effect of pretension on the performance of cable bolts and its optimisation in underground coal mines with various geological conditions. Int J Rock Mech Min Sci 152

Li X, Si G, Wei C, Oh J, Canbulat I (2023) Simulation of ductile fracture propagation using the elastoplastic phase-field damage method calibrated by ultrasonic wave velocity measurement. Int J Rock Mech Min Sci 161

Lin C, Xia C, Liu Z, Zhou C (2022) A comprehensive correlation study of structured soils in coastal area of South China about structural characteristics. J Mar Sci Eng 10(4):508

Liu HZ, Xie HQ, He JD, Xiao ML, Zhuo L (2017) Nonlinear creep damage constitutive model for soft rocks. Mech Time-Depend Mater 21(1):73–96

Liu Z, Zhou C, Li B, Zhang L, Liang Y (2020a) Effects of grain dissolution-diffusion sliding and hydro-mechanical interaction on the creep deformation of soft rocks. Acta Geotech 15(5):1219–1229

Liu Z, Zhou C, Su D, Du Z, Zhu F, Zhang L (2020b) Rheological deformation behavior of soft rocks under combination of compressive pressure and water-softening effects. Geotech Test J 43(3):737–757

Liu W, Chen J, Chen L, Luo Y, Shi Z, Wu Y (2022) Nonlinear deformation behaviors and a new approach for the classification and prediction of large deformation in tunnel construction stage: a case study. Eur J Environ Civ Eng 26(5):2008–2036

Maheshwari P (2021) Analysis of deformation of linear viscoelastic two layered laminated rocks. Int J Rock Mech Min Sci 141

Manchao H (2014) Latest progress of soft rock mechanics and engineering in China. J Rock Mech Geotech Eng 6(3):165–179

Mu W, Li L, Chen D, Wang S, Xiao F (2020) Long-term deformation and control structure of rheological tunnels based on numerical simulation and on-site monitoring. Eng Fail Anal 118

Ping C, Wen Y, Wang Y, Yuan H, Yuan B (2016) Study on nonlinear damage creep constitutive model for high-stress soft rock. Environ Earth Sci 75(10)

Pinyol NM, Vaunat J, Alonso EE (2007) A constitutive model for soft clayey rocks that includes weathering effects. Geotechnique 57(2):137–151

Potyondy DO (2007) Simulating stress corrosion with a bonded-particle model for rock. Int J Rock Mech Min Sci 44(5):677–691

Potyondy DO, Cundall PA (2004) A bonded-particle model for rock. Int J Rock Mech Min Sci 41(8):1329–1364

Song ZP, Yang TT, Jiang AN, Zhang DF, Jiang ZB (2016) Experimental investigation and numerical simulation of surrounding rock creep for deep mining tunnels. J South Afr Inst Min Metall 116(12):1181–1188

Song Z, Konietzky H, Herbst M (2019) Bonded-particle model-based simulation of artificial rock subjected to cyclic loading. Acta Geotech 14(4):955–971

Sun X, Zhao C, Tao Z, Kang H, He M (2021) Failure mechanism and control technology of large deformation for Muzhailing Tunnel in stratified rock masses. Bull Eng Geol Env 80(6):4731–4750

Tang H, Wang D, Huang R, Pei X, Chen W (2018) A new rock creep model based on variable-order fractional derivatives and continuum damage mechanics. Bull Eng Geol Env 77(1):375–383

Tao Z, Luo S, Kang H, Xie S, He M (2020) Analysis of deformation law and creep characteristics of carbonaceous slate in highway tunnel. J China Univ Min Technol 49(5):898–906

Wang M, Cai M (2020) A grain-based time-to-failure creep model for brittle rocks. Comput Geotech 119

Wang M, Cai M (2021a) A simplified model for time-dependent deformation of rock joints. Rock Mech Rock Eng 54(4):1779–1797

Wang MZ, Cai M (2021b) Numerical modeling of time-dependent spalling of rock pillars. Int J Rock Mech Min Sci 141

Wang M, Cai M (2022a) Modeling of time-dependent deformation of jointed rock mass. Rock Mech Rock Eng 55(4):2049–2070

Wang M, Cai M (2022b) Numerical modeling of stand-up time of tunnels considering time-dependent deformation of jointed rock masses. Rock Mech Rock Eng 55(7):4305–4328

Wang J-g, Sun Q-l, Liang B, Yang P-j, Yu Q-r (2020) Mudstone creep experiment and nonlinear damage model study under cyclic disturbance load. Sci Rep 10(1)

Wei S, Shen J, Yang W, Li Z, Di S, Ma C (2019) Application of the renormalization group approach for permeability estimation in digital rocks. J Petrol Sci Eng 179:631–644

Xia C, Liu Z, Zhou C (2021a) Burger's bonded model for distinct element simulation of the multi-factor full creep process of soft rock. J Mar Sci Eng 9(9)

Xia C, Zhou C, Zhu F, Liu Z, Cui G (2021b) The critical indicator of red-bed soft rocks in deterioration process induced by water basing on renormalization group theory. Appl Sci-Basel 11(17)

Xiong L, Liu Y, Yuan W, Huang S, Liu H, Li H, Lin F, Pan Y (2020) Experimental and numerical study on the cracking characteristics of repetitive electrohydraulic discharge shock waves. J Phys D-Appl Phys 53(49)

Xu T, Tang C-A, Zhao J (2012) Modeling of rheological deformation of inhomogeneous rock and associated time-dependent response of tunnels. Int J Geomech 12(2):147–159

Xue Y, Ma X, Qiu D, Yang W, Li X, Kong F, Zhou B, Qu C (2021) Analysis of the factors influencing the nonuniform deformation and a deformation prediction model of soft rock tunnels by data mining. Tunn Undergr Space Technol 109

Xue Y, Liu J, Ranjith PG, Zhang ZZ, Gao F, Wang SH (2022) Experimental investigation on the nonlinear characteristics of energy evolution and failure characteristics of coal under different gas pressures. Bull Eng Geol Environ 81(1)

Yang S-Q, Tao Y, Xu P, Chen M (2019) Large-scale model experiment and numerical simulation on convergence deformation of tunnel excavating in composite strata. Tunn Undergr Space Technol 94

Yu J, Liu G, Cai Y, Zhou J, Liu S, Tu B (2020) Time-dependent deformation mechanism for swelling soft-rock tunnels in coal mines and its mathematical deduction. Int J Geomech 20(3)

Zhang X, He M, Wang F, Li G, Xu S, Tao Z (2020) Study on the large deformation characteristics and disaster mechanism of a thin-layer soft-rock tunnel. Adv Civ Eng 2020

Zhang X, Lin H, Wang Y, Yong R, Zhao Y, Du S (2021) Damage evolution characteristics of saw-tooth joint under shear creep condition. Int J Damage Mech 30(3):453–480

Zhou CY, Zhu FX (2010) An elasto-plastic damage constitutive model with double yield surfaces for saturated soft rock. Int J Rock Mech Min Sci 47(3):385–395

Zhou C, Liang N, Liu Z (2019) Fractal characteristics of compression failure of red soft rock and cascading failure process. Rock Soil Mech 40(S1):21–31